

5-1-2015

# Incorporating Relaxivities to More Accurately Reconstruct MR Images

Muge Karaman

*University of Illinois at Chicago*

Iain P. Bruce

*Duke University*

Daniel B. Rowe

*Marquette University, [daniel.rowe@marquette.edu](mailto:daniel.rowe@marquette.edu)*

---

Accepted version. *Magnetic Resonance Imaging*, Vol. 33, No. 4 (May 2015): 374-384. [DOI](#). © 2015 Elsevier Inc. Used with permission.

NOTICE: this is the author's version of a work that was accepted for publication in *Magnetic Resonance Imaging*. Changes resulting from the publishing process, such as peer review, editing, corrections, structural formatting, and other quality control mechanisms may not be reflected in this document. Changes may have been made to this work since it was submitted for publication. A definitive version was subsequently published in *Magnetic Resonance Imaging*, Vol. 33, No. 4 (May 2015): 374-384. [DOI](#).

# Incorporating Relaxivities to More Accurately Reconstruct MR Images

Muge Karaman

*Center for MR Research, University of Illinois at Chicago,  
Chicago, IL*

Iain P. Bruce

*Duke/UNC Brain Imaging and Analysis Center, Duke University,  
Durham, NC*

Daniel B. Rowe

*Department of Mathematics, Statistics, and Computer Science,  
Marquette University,  
Department of Biophysics, Medical College of Wisconsin,  
Milwaukee, WI*

## **Abstract**

**Purpose:** To develop a mathematical model that incorporates the magnetic resonance relaxivities into the image reconstruction process in a single step.

**Materials and Methods:** In magnetic resonance imaging, the complex-valued measurements of the acquired signal at each point in frequency space are expressed as a Fourier transformation of the proton spin density weighted by Fourier encoding anomalies:  $T_2^*$ ,  $T_1$ , and a phase determined by magnetic field inhomogeneity ( $\Delta B$ ) according to the MR signal equation. Such anomalies alter the expected symmetry and the signal strength of the  $k$ -space

observations, resulting in images distorted by image warping, blurring, and loss in image intensity. Although  $T_1$  on tissue relaxation time provides valuable quantitative information characteristics, the  $T_1$  recovery term is typically neglected by assuming a long repetition time. In this study, the linear framework presented in the work of [Rowe et al., 2007](#), and of [Nencka et al., 2009](#) is extended to develop a Fourier reconstruction operation in terms of a real-valued isomorphism that incorporates the effects of  $T_2^*$ ,  $\Delta B$ , and  $T_1$ . This framework provides a way to precisely quantify the statistical properties of the corrected image-space data by offering a linear relationship between the observed frequency space measurements and reconstructed corrected image-space measurements. The model is illustrated both on theoretical data generated by considering  $T_2^*$ ,  $T_1$ , and/or  $\Delta B$  effects, and on experimentally acquired fMRI data by focusing on the incorporation of  $T_1$ . A comparison is also made between the activation statistics computed from the reconstructed data with and without the incorporation of  $T_1$  effects.

**Result:** Accounting for  $T_1$  effects in image reconstruction is shown to recover image contrast that exists prior to  $T_1$  equilibrium. The incorporation of  $T_1$  is also shown to induce negligible correlation in reconstructed images and preserve functional activations.

**Conclusion:** With the use of the proposed method, the effects of  $T_2^*$  and  $\Delta B$  can be corrected, and  $T_1$  can be incorporated into the time series image-space data during image reconstruction in a single step. Incorporation of  $T_1$  provides improved tissue segmentation over the course of time series and therefore can improve the precision of motion correction and image registration.

**Keywords:** Magnetic resonance imaging (MRI), functional MRI (fMRI), MR relaxivities, longitudinal relaxation time ( $T_1$ ), image reconstruction, correction

## 1. Introduction

In magnetic resonance imaging (MRI), data is acquired in the spatial frequency domain and reconstructed through an inverse Fourier transform, into images of the object in the image domain. Thus, the measured  $k$ -space data, encoded in time, is generally expected to be the Fourier transform of the proton spin density. However, in the process of Fourier encoding in echo planar imaging (EPI), the detected MRI signal is subject to the MR relaxivities,  $T_2^*$  and  $T_1$ , as well as magnetic field inhomogeneity,  $\Delta B$ , commonly referred to as Fourier anomalies. The physical mechanisms behind the Fourier encoding process causes image artifacts or image distortions. One such effect is the one caused by acquiring measurements of  $k$ -space at different times after the RF excitation pulse. Due to the non-instantaneous acquisition of each  $k$ -space line, the first points sampled have a lower  $T_2^*$  weighting than the subsequent points. Considering that the "ideal" image would be reconstructed from the "ideal"  $k$ -space measurements,

in which every point is sampled with the exact same weighting, the "actual" acquired  $k$ -space measurements in practice are scaled according to the time by a factor determined by  $T_2^*$ .<sup>1,2</sup> As such, the "actual" reconstructed image, which is obtained by an inverse Fourier transformation of the "actual"  $k$ -space measurements, has a blurring effect in the phase encoding direction as a result of the inverse Fourier transformation of this weighting pattern. Moreover, the differences in magnetic susceptibility between tissues or magnetic materials lead to incorrect sampling of  $k$ -space by introducing errors in the gradients. Thus, the point in  $k$ -space that is believed to be sampled is not the actual location. As such, magnetic field inhomogeneities incur spatial distortions including image warping and phase generation. Although the weighting through  $T_1$  is not affected by the non-instantaneous sampling of  $k$ -space, it can modulate the MR signal resulting in signal loss and image weighting that depend on the tissue characteristics. The artifacts resulting from  $T_2^*$  relaxation during sampling, the inhomogeneities in the magnetic field, and the alteration in the signal arising from the longitudinal relaxation can be considered as  $T_2^*$ ,  $\Delta B$ , and  $T_1$  effects, respectively,

Correcting the image warping effects of both the static and dynamic magnetic field inhomogeneities,<sup>3-7</sup> and the  $T_2^*$  blurring effect<sup>8-11</sup> in EPI sequences have been active areas of research in brain imaging. Despite such efforts for correcting  $T_2^*$  and  $\Delta B$  effects, conventional studies do not account for a recovery of the longitudinal relaxation time; instead they use the standard assumption of a long repetition time. However, this assumption is not always valid, and the signal amplitude becomes dependent on  $T_1$  when performing fast repetitive image excitations with incomplete recovery of the longitudinal magnetization. Moreover,  $T_1$  relaxation time provides a robust contrast mechanism for distinguishing tissue type.<sup>12</sup> This quantitative knowledge of tissue characteristics, which can be extracted from the data acquired during the transient state prior to  $T_1$  equilibrium, can be incorporated into the reconstructed image-space time series data. It has been suggested in previous studies that the image registration performance can be improved with increased tissue contrast.<sup>13-16</sup> Therefore,  $T_1$  incorporated time series images, which would have appreciably higher tissue contrast, can potentially lead to improved image registration.

As noted before, the Fourier anomalies appear as exponential terms in the traditional signal equation, and therefore the observed  $k$ -space measurements can be considered as the Fourier transform of the proton spin density, weighted by the Fourier anomalies. Since the  $k$ -space measurements are subject to the effects of such weighting during data acquisition, these effects can be accounted for separately or simultaneously in the process of Fourier reconstruction.

In order to relate the signal and noise characteristics of  $k$ -space measurements to reconstructed voxel measurements, the complex-valued matrix application of the inverse Fourier transformation was described through a real-valued isomorphism by Rowe et al.<sup>17</sup> Representing the Fourier reconstruction as a single matrix operator formed the basis for the study in<sup>18</sup> where a mathematical framework, AMMUST- $k$  (A Mathematical Model for Understanding the STatistical effects of  $k$ -space preprocessing), was developed to represent various spatial processing operations performed on acquired spatial frequencies in terms of real-valued linear isomorphisms. Representing the reconstruction and image processing operations in this way made it possible to directly compute the exact covariance structure, and ultimately correlation induced into the image-space data, which can result in misleading conclusions in fcMRI and fMRI studies.<sup>18-20</sup>

In this manuscript, we expand upon the AMMUST- $k$  framework by modifying the real-valued Fourier reconstruction (FR) operator in such a way that it can account for the effects of  $T_2^*$ ,  $\Delta B$ , and  $T_1$  on the image-space data. As noted before, the measured "actual"  $k$ -space data is scaled according to time that has elapsed since the RF excitation pulse and the factor determined by the terms include  $T_2^*$ ,  $\Delta B$ , and  $T_1$ . As such, we first develop a real-valued Fourier encoding (FE) operator that considers such weighting, then, we create the modified FR operator by inverting the modified FE operator to account for the encoding effects in image space. The use of a modified FR operator within this framework makes it possible to more accurately reconstruct the image space voxel values from measured spatial frequencies, and also precisely quantify the statistical effects of such correction on the reconstructed data.

The linear Fourier reconstruction operators are first developed by considering different combinations of the Fourier anomalies and

examples of each anomaly are shown on a small  $8 \times 8$  data set. The Fourier operators are then used to theoretically examine the image space data associated with the effects of the Fourier anomalies on a  $96 \times 96$  digital phantom. The exact mean and induced correlations modified by the adjusted FR operators on both complex-valued and magnitude-squared data are also illustrated by using the proposed model. The results of the proposed FE anomaly correction framework is also illustrated on acquired experimental human subject fMRI data by focusing on the incorporation of the longitudinal relaxation time,  $T_1$ . Finally, a comparison is made between the activation statistics computed from the reconstructed data with and without the incorporation of  $T_1$  effects with the use of both conventional magnitude-only<sup>21</sup> and newer complex-valued fMRI activation models.<sup>22-25</sup>

## 2. Theory

### 2.1. Complex-valued Image Reconstruction in fMRI

In fMRI, complex-valued measurements are acquired discretely in time corresponding to two-dimensional spatial frequency measurements. The measurements are then reconstructed into a complex-valued image by applying the complex-valued inverse Fourier transformation. Although the original object, proton spin density, is real-valued, imperfections in the imaging process lead to a complex-valued image.

When the complex-valued Fourier reconstruction is described through a real-valued isomorphism,<sup>17</sup> a vector of the reconstructed image,  $y$ , can be written as the product of a FR operator,  $\Omega$ , with a vector of the observed  $k$ -space observation,  $s$ , by

$$y = \Omega s. \quad (1)$$

Similarly, the vector of the  $k$ -space observation,  $s$ , can be written as the product of a FE operator,  $\bar{\Omega} = \Omega^{-1}$ , with a vector of the reconstructed image,  $y$ , as

$$s = \bar{\Omega}y. \quad (2)$$

In Eqs. (1) and (2),  $y = (y_R', y_I')'$  is a  $2p \times 1$  vector with the real parts of  $p$  image values,  $y_R = (y_{R1}, \dots, y_{Rp})'$ , stacked above the imaginary parts of  $p$  image values,  $y_I = (y_{I1}, \dots, y_{Ip})'$ , for an  $m \times n$  image of  $p = mn$  voxels. Similarly,  $s = (s_R', s_I')'$  is a  $2p \times 1$  vector with  $p$  real parts,  $s_R = (s_{R1}, \dots, s_{Rp})'$ , stacked above  $p$  imaginary parts,  $s_I = (s_{I1}, \dots, s_{Ip})'$ , for a Cartesian acquisition of  $k$ -space. Thus, the FR and FE operators,  $\Omega$  and  $\bar{\Omega}$ , have dimensions of  $2p \times 2p$ . The Cartesian FR operator can be represented as

$$\Omega = \begin{pmatrix} \text{Re}(\Omega_C) & -\text{Im}(\Omega_C) \\ \text{Im}(\Omega_C) & \text{Re}(\Omega_C) \end{pmatrix}, \quad (3)$$

where  $\text{Re}(\cdot)$  and  $\text{Im}(\cdot)$  denote the real and imaginary parts of their respective arguments. The matrix  $\Omega_C$  is defined as the Kronecker product of the matrices,  $\Omega_x$  and  $\Omega_y$ , as  $\Omega_C = \Omega_x \otimes \Omega_y$ , where the matrices  $\Omega_x$  and  $\Omega_y$  Fourier transform the columns and the rows of the acquired  $k$ -space measurements, respectively. The  $jk^{\text{th}}$  element of the FR operator  $\Omega_x$  can be written as  $(\Omega_x)_{jk} = w^{((-n/2)+(j-1))((-n/2)+(k-1))}$ , where  $j$  and  $k$  are the indices from 1 to  $n$  and  $w = (1/n)\exp(i2\pi/n)$ . The matrix  $\Omega_y$  follows similarly with  $n$  replaced by  $m$ . The Fourier encoding operator,  $\bar{\Omega}$ , has a similar skew symmetric form to  $\Omega$  where  $w = \exp(-i2\pi/n)$ . The operators,  $\Omega$  and  $\bar{\Omega}$ , will be considered as the standard FR and FE operators as they do not account for any Fourier anomalies.

As the real-valued spatial frequency vector,  $s$ , contains complex-values, the application of the FR operator in Eq. (1) produces a covariance between the real measurements, between the imaginary measurements, and between the real and imaginary measurements. If the  $k$ -space vector,  $s$ , has a covariance matrix,  $\Gamma$ , then the covariance matrix of the reconstructed image,  $y$ , becomes

$$\text{cov}(y) = \Omega\Gamma\Omega', \quad (4)$$

where the operator  $'$  denotes the transpose of a matrix.

To produce the required  $k$ -space vector,  $s$ , the acquired  $k$ -space array, which is observed as a pairing of real and imaginary component of each frequency can be reordered by reversing the alternating rows of measurements and segregating real and imaginary observations through permutation matrices,  $P_A$  and  $P_S$ . Since the  $k$ -space data includes extra points acquired during the phase encoding blips in echo planar imaging, the acquired measurements also needs to be censored by the censoring matrix,  $P_E$ . Additionally, Nyquist ghosting can be corrected through a series of linear operators that reorders to group the real and imaginary observations from each line together ( $P_R$ ), Fourier transform each row ( $\Omega_R$ ), shift the phase of the each transformed row ( $\Phi_N$ ), and finally apply the inverses of  $\Omega_R$  and  $P_R$ . These  $k$ -space operators together with additional operators that can include Fourier homodyne interpolation,  $H$ , zero-filling,  $F$ , apodization,  $A$ , and explicit image space smoothing operator,  $S$ , can be combined into a single operator,  $O$ , that signifies the series of all linear operators applied to  $s$ .<sup>18</sup> Therefore, the reconstruction in [Eq. \(1\)](#) simplifies to

$$y = Os, \quad (5)$$

where  $O$  represents a multiplication of operators applied throughout the image reconstruction process,

$$O = S\Omega A F H P_R^{-1} \Omega_R^{-1} \Phi_N \Omega_R P_R P_S P_A P_E. \quad (6)$$

If  $E(s) = s_0$  and  $\Gamma = \text{cov}(s)$ , then mean and covariance of the reconstructed image vector,  $y$ , are altered by the final operator,  $O$ , to become

$$E(y) = Os_0$$

and

$$\text{cov}(y) = O\Gamma O'. \quad (7)$$



The correlation structure between voxels in  $y$  can be calculated from  $cov(y)$  by

$$corr(y) = D^{-1/2} O \Gamma O' D^{-1/2}, \quad (8)$$

where  $D$  is a diagonal matrix of the variances drawn from the diagonal of the covariance matrix,  $O \Gamma O'$ , and the  $-1/2$  superscript denotes that the diagonal elements are inverted after taking the square root. The covariance matrices of both the spatial frequencies and the reconstructed image-space values include the following covariance pairs: real by real, imaginary by imaginary, and real by imaginary components of  $s$  and  $y$ , respectively.

An assumption of normality allows the derivation of the covariance of the square of the magnitude data from the covariance matrix,  $cov(y) = O \Gamma O'$ .<sup>17,18</sup> Both magnitude-squared and complex-valued data can be used to analyze changes made to the acquired correlation structures as the correlation of magnitude-squared data is asymptotically equivalent to the magnitude-only correlation and linear in nature.

## 2.2. Acquired $k$ -space Signal and Fourier Anomalies

Under the assumption that the complex-valued matrix of two dimensional spatial frequencies is measured instantaneously at the echo time, TE, the acquired  $k$ -space signal in an EPI sequence can be expressed through the MR signal equation,

$$\begin{aligned} s(k_x, k_y) &= \int_{-\infty}^{\infty} \int_{-\infty}^{\infty} M_0(x, y) (1 \\ &- e^{-TR/T_1(x,y)}) e^{-TE/T_2^*(x,y)} e^{i\gamma \Delta B(x,y)TE} e^{-i2\pi(k_x x + k_y y)} dx dy, \end{aligned} \quad (9)$$

where TR is the repetition time and  $M_0(x, y)$  is the proton spin density.

Since the signal for different points in  $k$ -space is measured at different times, the  $k$ -space observation process occurs over a finite duration of time and the signal equation in [Eq. \(9\)](#) can be more accurately expressed as

$$s(k_x, k_y) = \int_{-\infty}^{\infty} \int_{-\infty}^{\infty} M_0(x, y) (1 - e^{-TR/T_1(x,y)}) e^{-t/T_2^*(x,y)} e^{i\gamma\Delta B(x,y)t} e^{-i2\pi(k_x x + k_y y)} dx dy, \quad (10)$$

where the  $k$ -space point  $(k_x, k_y)$  is sampled at time  $t=t(k_x, k_y)$ . As the variable  $t=t(k_x, k_y)$  varies for each  $k$ -space measurement, both  $T_2^*$  and  $\Delta B$  break the Hermitian symmetry of the  $k$ -space observations, and could therefore cause artifacts and distortions in the reconstructed images. Moreover, the longitudinal relaxation time,  $T_1$ , causes changes in signal intensity depending on the tissue characteristics.

In conventional studies, the term  $(1-\exp(-TR/T_1))$  in [Eq. \(10\)](#) is assumed to be approximately 1, by choosing TR to be much greater than  $T_1$ . This reduces [Eq. \(10\)](#) to depend only on  $T_2^*$  by

$$s(k_x, k_y) = \int_{-\infty}^{\infty} \int_{-\infty}^{\infty} M_0(x, y) e^{-t/T_2^*(x,y)} e^{i\gamma\Delta B(x,y)t} e^{-i2\pi(k_x x + k_y y)} dx dy, \quad (11)$$

and thus leads to  $T_2^*$ -weighted images.

The assumption of an infinite TR however can never be reached directly since the goal is to image the brain as quickly as possible, thus fast acquisitions are needed. The neglected term,  $(1-\exp(-TR/T_1))$ , therefore takes non-negligible values with the parameter settings that are commonly used in fMRI experiments. Presented in [Table 1](#) are the values that  $(1-\exp(-TR/T_1))$  outputs when the relaxation parameter

values of gray matter and white matter tissues measured at 3.0 T<sup>26</sup> and two commonly used TR values, 1000 ms and 2000 ms, are used. It is of note here that the value of  $(1-\exp(-TR/T_1))$  is expected to be slightly lower at 7.0 T which has been widely used in high-field fMRI for study of the human brain. Furthermore, the variations in the value of TR have an essential effect on the control of image contrast characteristics. As such, accounting for  $T_1$  effects has the potential of retaining the image contrast over the time series that exists prior to  $T_1$  equilibrium. The regular FR operator,  $\Omega$ , is thus modified with the aim of analyzing and accounting for the effects of Fourier anomalies:  $T_2^*$ ,  $\Delta B$ , and  $T_1$ .

**Table 1.**  $T_1$  exponential term values at 3.0 T.

$1-\exp(-TR/T_1(x,y))$	TR = 1000 ms	TR = 2000 ms
GM ( $T_1 = 1331$ ms.)	0.5283	0.7750
WM ( $T_1 = 832$ ms.)	0.6994	0.9096

### 2.3. Incorporating MR Relaxivities to Fourier Reconstruction Process

In this section, we develop a modified Fourier image reconstruction operator that produces the "ideal" image space vector,  $y_{Id}$ , from the "actual" measured  $k$ -space vector,  $s_{Act}$ , that is affected by the exponential terms for  $T_2^*$ ,  $\Delta B$ , and  $T_1$  during the Fourier encoding process. Consider that the "ideal" image space vector,  $y_{Id}$ , would be constructed from the "ideal"  $k$ -space vector,  $s_{Id}$ , that is not affected by FE anomalies and the "actual" measured signal,  $s_{Act}$ , that we acquire in practice is scaled according to a weighting determined by FE anomalies.

As each  $k$ -space measurement is approximately expressed as the forward Fourier transform of the spin density, weighted by the MR relaxivities and the magnetic field inhomogeneities at a single point in  $k$ -space, we can first incorporate the exponential terms for  $T_2^*$ ,  $T_1$ , and  $\Delta B$  into the FE operator,  $\bar{\Omega}$ . Then, we construct the modified FR operator by taking the inverse of the modified FE operator matrix.

As with the Cartesian Fourier reconstruction operator given in [Eq. \(3\)](#), the Cartesian FE operator is expressed as

$$\Omega = \begin{pmatrix} \text{Re}(\bar{\Omega}_C) & -\text{Im}(\bar{\Omega}_C) \\ \text{Im}(\bar{\Omega}_C) & \text{Re}(\bar{\Omega}_C) \end{pmatrix}, \quad (12)$$

where  $\bar{\Omega}_C$  is defined as  $\bar{\Omega}_C = \bar{\Omega}_x \otimes \bar{\Omega}_y$ , and the  $jk^{\text{th}}$  element of  $\bar{\Omega}_x$  can be written as  $(\bar{\Omega}_x)_{jk} = w^{((-n/2)+(j-1))((-n/2)+(k-1))}$  where  $j$  and  $k$  are the indices from 1 to  $n$  when  $w = \exp(-i2\pi/n)$ .

Regardless of the relaxation times or  $\Delta B$  that cause the weighting difference, in the general case, we can describe the weighting of the MR signal at each point with a two-dimensional array,  $W$ , as

$$\begin{aligned} W(k_x, k_y, x, y) \\ = (1 \\ - e^{-TR/T_1(x,y)}) e^{-t(k_x, k_y)/T_2^*(x,y)} e^{i\gamma \Delta B(x,y)t(k_x, k_y)}. \end{aligned} \quad (13)$$

Two dimensional FE anomaly weighting function,  $W$ , can be constructed as

$$W(k_x, k_y, x, y) = \begin{bmatrix} W(1,1,1,1) & \cdots & W(m,n,1,1) \\ \vdots & \ddots & \vdots \\ W(1,1,m,n) & \cdots & W(m,n,m,n) \end{bmatrix},$$

for an  $m \times n$  image.

In order to achieve the ideal image space vector,  $y_{Id}$ , after reconstruction, we first modify  $\bar{\Omega}$  in [Eq. \(12\)](#), by including  $W$  into the real-valued isomorphism. The modified FE operator,  $\bar{\Omega}_a$ , can be created by first performing an element-wise multiplication of the Kronecker product,  $\bar{\Omega}_a$ , by the FE anomaly weighting function as

$$\bar{\Omega}_{C,a} = (\bar{\Omega}_x \otimes \bar{\Omega}_y) \circ W(k_x, k_y, x, y), \quad (14)$$

where  $\circ$  represents an element-wise Hadamard product. Finally, the modified FE operator,  $\bar{\Omega}_a$ , can be expressed as

$$\bar{\Omega}_a = \begin{pmatrix} \text{Re}(\bar{\Omega}_{C,a}) & -\text{Im}(\bar{\Omega}_{C,a}) \\ \text{Im}(\bar{\Omega}_{C,a}) & \text{Re}(\bar{\Omega}_{C,a}) \end{pmatrix}. \quad (15)$$

The modified FR operator,  $\Omega_a$ , can then be calculated by  $\Omega_a = \bar{\Omega}_a^{-1}$ .

With the modified FR operator that accounts for the effects of the FE anomalies, the operator,  $O$ , in [Eq. \(6\)](#) can be updated to

$$O_a = S\Omega_a A F H P_R^{-1} \Omega_R^{-1} \Phi_N \Omega_R P_R P_S P_A P_E. \quad (16)$$

The complete process given in [Eq. \(5\)](#) can be written in such a way that the operator,  $O_a$ , reconstructs the "actual" measured  $k$ -space vector,  $s_{Act}$ , into the "ideal" corrected image space vector,  $y_{Id}$ , as

$$y_{Id} = O_a s_{Act}. \quad (17)$$

The inclusion of  $T_2^*$ ,  $\Delta B$ , and  $T_1$  finely alters the structure of the standard FE and FR operators,  $\bar{\Omega}$  and  $\Omega$  to arrive at  $\bar{\Omega}_a$  and  $\Omega_a$ . The alterations caused by the FE anomalies in the FE operator, and in the FR operator that accounts for such alterations can be better seen in a low-dimensional example than a real size data set. Presented for an  $8 \times 8$  example, the  $128 \times 128$  arrays in [Figs. 1\(a\) and 1\(c\)](#) are the FE and FR operators that either do not account for any terms (standard operators), or separately accounts for the  $T_2^*$  decay,  $\Delta B$  in the frequency encoding direction, and the  $T_1$  recovery term.  $T_2^*$  and  $T_1$  maps were considered in the example map which were scaled to values from 80 to 100 ms and 800 to 1000 ms inside the phantom, respectively. The  $\Delta B$  term was modeled as a linear gradient ranging

from 0 to  $2.5 \times 10^{-6}$  T. It can be seen in the second and third panels of [Figs. 1\(a\) and 1\(c\)](#) that the incorporation of  $T_2^*$  and  $T_1$  recovery causes amplitude change in the modified FE and FR operators for the considered TR and TE values. One can observe that the modified FE operator that includes  $T_2^*$  and  $T_1$ , given in the second and third panels of [Fig. 1\(a\)](#), are visually different from the standard FE operator. Since  $\exp(-t/T_2^*)$  in [Eq. \(13\)](#) converges to 0 for the voxels that have small  $T_2^*$  values, the element values of the modified FE operator in the second panel tend toward zero in the portions that correspond to these voxels with low  $T_2^*$  value. Moreover, the operators that incorporate  $\Delta B$  effects that are given in the fourth panel of [Fig. 1\(a\) and 1\(c\)](#) appear to be clearly different than the standard arrays as a result of the linear gradient change in magnetic field.

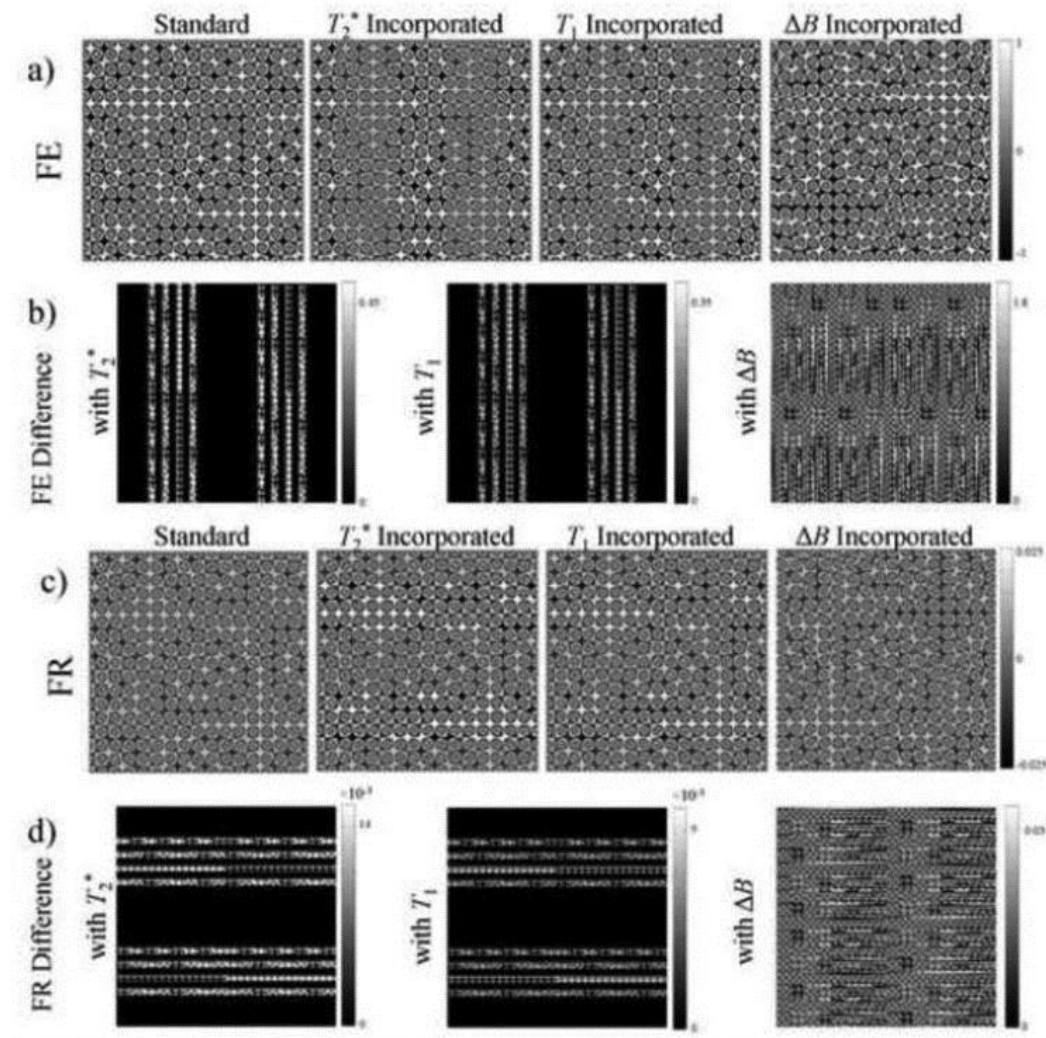


**Fig.1.** a) and c) Standard FE and FR operators,  $\bar{\Omega}$  and  $\Omega$ , in the first panel; modified FE and FR operators,  $\bar{\Omega}_a$  and  $\Omega_a$ , that separately accounts for the effects of  $T_2^*$ ,  $T_1$ , or  $\Delta B$  in the second, third, and fourth panels, respectively. Absolute difference maps between  $\bar{\Omega}$  and  $\bar{\Omega}_a$  and between  $\Omega$  and  $\Omega_a$  are given in b) and d) for the cases of  $T_2^*$ ,  $T_1$ , or  $\Delta B$  incorporation in the first, second, and third panels, respectively.

For a better illustration of the effects of the anomalies on the FE and FR operators, the difference maps of the standard FE and FR operators with their modified versions that separately accounts for the effects of  $T_2^*$ ,  $T_1$ , and  $\Delta B$  are given in [Figs. 1\(b\) and 1\(d\)](#), respectively. It can be observed from the first and second panels of [Figs. 1\(b\) and 1\(d\)](#) that most noticeable difference occurs from the  $T_2^*$  and  $T_1$  weighting of the voxels that have low  $T_2^*$  and high  $T_1$  values. This appears as horizontal and vertical bands in the difference maps of the FE and FR operators, respectively. The third panel of [Fig. 1\(b\)](#) show that the linear gradient changes in magnetic field causes changes in every element of the standard FE operator as its effect is not voxel-dependent. A similar modification can also be observed in the FR operator that accounts for the  $\Delta B$  effect given in the third panel of [Fig. 1\(d\)](#).

### 3. Methods

#### 3.1. Theoretical Illustration

To theoretically illustrate the performances of the developed Fourier reconstruction operators, a single-slice of data was generated from a noiseless digital brain phantom. In order to replicate the process of acquiring data from an MRI scanner with a standard EPI pulse sequence, a single time point complex-valued spatial frequency data,  $s(k_x, k_y)$ , was generated using the MR signal equation given in [Eq. \(10\)](#) under various cases in which  $T_2^*$ ,  $T_1$ , and/or  $\Delta B$  is considered. Simulated at 3 T, the proton spin density,  $M_0$ , in a  $96 \times 96$  phantom in [Fig. 2\(a\)](#) was used with model  $T_2^*$  and  $T_1$  values that vary from 42 to 2200 ms for  $T_2^*$  and from 832 to 4000 ms for  $T_1$ , as given in [Figs. 2\(b\) and 2\(c\)](#).<sup>26</sup> The  $\Delta B$  was considered as a left to right gradient from 0 to  $2.5 \times 10^{-6}$  T, as shown in [Fig. 2\(d\)](#). The timing of the  $k$ -space sampling scheme was as in a standard EPI pulse sequence for a  $96 \times 96$  acquisition matrix, with a bandwidth of 250 kHz, an effective echo spacing of 0.72 ms, an echo time of 50 ms, and a TR of 1 s. The phase



encoding direction was assumed to be oriented as posterior to anterior (bottom to top in images).

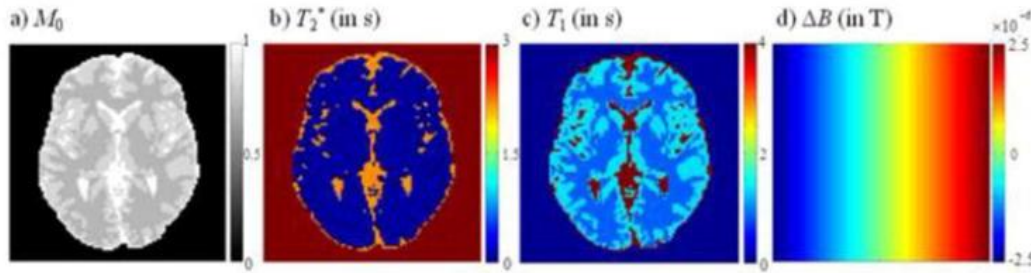


**Fig. 2.** Parameters considered in theoretical calculations. a) Proton spin density,  $M_0$ , (GM:0.83, WM:0.71, CSF:1), b) intra-acquisition decay,  $T_2^*$  (GM:0.042 s, WM:0.049 s, CSF:2.2s), c) longitudinal relaxation time,  $T_1$  (GM:1.331 s, WM:0.832 s, CSF:4s), d)  $B$ -field inhomogeneity,  $\Delta B$  (left to right linear gradient changing from 0 to  $2.5 \times 10^{-6}$  Tesla).

In our calculations for the theoretical illustration, we consider the  $k$ -space operators:  $P_E$ ,  $P_A$ ,  $P_S$ ,  $P_R$ ,  $\Omega_R$ ,  $\Phi_N$ ,  $\Omega_R^{-1}$ ,  $P_R^{-1}$  and the FR operator,  $\Omega$  or  $\Omega_a$ , depending on our analysis. Thus, the altered mean and the induced covariance matrix by the applied operators can be calculated according to [Eq. \(7\)](#) by

$$E(y_{Id}) = \Omega_a P_R^{-1} \Omega_R^{-1} \Phi_N \Omega_R P_R P_S P_A P_E S_{Act}$$

and

$$\begin{aligned} \text{cov}(y_{Id}) &= (\Omega_a P_R^{-1} \Omega_R^{-1} \Phi_N \Omega_R P_R P_S P_A P_E) \Gamma \\ & (P_E' P_A' P_S' P_R' \Omega_R' \Phi_N' (\Omega_R^{-1})' (P_R^{-1})' \Omega_a'). \end{aligned} \quad (18)$$

It should be noted that if  $\Gamma = I$ , then [Eq. \(18\)](#) reduces to

$$\text{cov}(y_{Id}) = \Omega_a \Omega_a', \quad (19)$$

since when each of the operators, except  $\Omega_a$ , in [Eq. \(18\)](#) are multiplied by their transposes, the products yield identity matrices. Therefore,



the altered covariance and correlations will only result from the use of the modified FR operator,  $\Omega_a$ .

In order to examine the effects of FE anomalies on the reconstructed image space data, we use the data that is generated by considering the individual and sequential effects of  $T_2^*$ ,  $\Delta B$ , and  $T_1$  in the frequency space. Then, we perform the Fourier reconstruction with the use of the standard FR operator,  $\Omega$ , to visually illustrate the alterations that are caused by the FE anomalies if they are not accounted for. Finally, we perform the Fourier reconstruction with the use of the proposed modified FR operator,  $\Omega_a$ , on the same data set in order to present the performance of  $\Omega_a$  in accounting for such effects. Presented in [Fig. 3](#) are the magnitude, phase, real, and imaginary images that are reconstructed from the data sets generated with the effects of  $T_2^*$  in [Figs. 3\(a<sub>1</sub>\)](#), and [3\(a<sub>2</sub>\)](#), the effects of  $\Delta B$  in [Figs. 3\(b<sub>1</sub>\)](#), and [3\(b<sub>2</sub>\)](#), the effects of  $T_1$  in [Figs. 3\(c<sub>1</sub>\)](#), and [3\(c<sub>2</sub>\)](#), and finally the combined effects of  $T_2^*$ ,  $\Delta B$ , and  $T_1$  in [Figs. 3\(d<sub>1</sub>\)](#), and [3\(d<sub>2</sub>\)](#). [Figs. 3\(a<sub>1</sub>\)](#), [3\(b<sub>1</sub>\)](#), [3\(c<sub>1</sub>\)](#), and [3\(d<sub>1</sub>\)](#) show the images that are reconstructed with the use of the standard FR operator,  $\Omega$ , whereas [Figs. 3\(a<sub>2</sub>\)](#), [3\(b<sub>2</sub>\)](#), [3\(c<sub>2</sub>\)](#), and [3\(d<sub>2</sub>\)](#) illustrate the images that are reconstructed with the use of the modified FR operator,  $\Omega_a$ . In this manuscript, we denote the images as "standard-reconstructed" when the standard FR operator is used for reconstruction while we denote images as "modified-reconstructed" when the FR operator, modified to correct the effects of the respective FE anomaly, is used. When generating data for the results presented in [Fig. 3](#), the "true" magnitude of each image is assumed to be the proton spin density as given in [Fig. 2\(a\)](#), and the phase is originally assumed to be zero throughout the image.

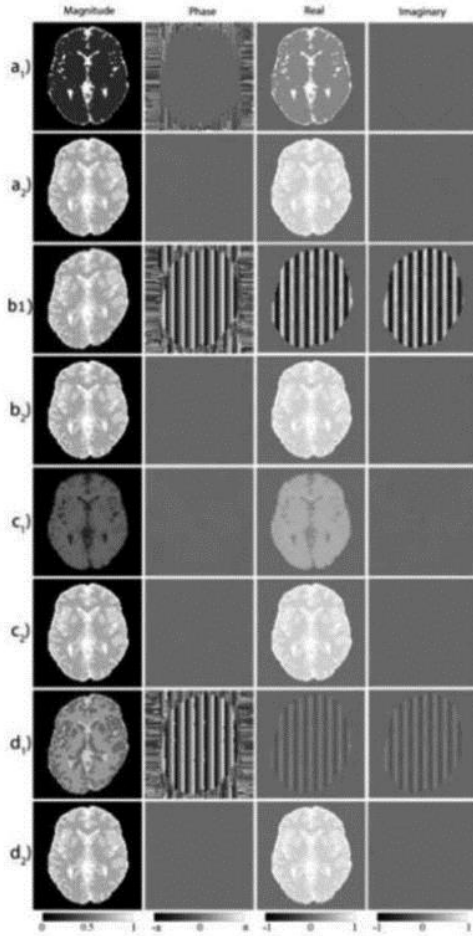


**Fig.3.** Reconstructed magnitude, phase, real, and imaginary images from the frequency space data that is generated with the effects of the following FE anomalies:  $T_2^*$  in  $a_1$  and  $a_2$ ,  $\Delta B$  in  $b_1$  and  $b_2$ ,  $T_1$  in  $c_1$  and  $c_2$ , and  $T_2^*$ ,  $\Delta B$ , and  $T_1$  in  $d_1$  and  $d_2$ . The images on the rows of  $a_1$ ,  $b_1$ ,  $c_1$ , and  $d_1$  are standard-reconstructed whereas the images on the rows of  $a_2$ ,  $b_2$ ,  $c_2$ , and  $d_2$  are modified-reconstructed from the data.

The reconstructed image results that are presented in [Figs. 3\(a<sub>1</sub>\) and 3\(a<sub>2</sub>\)](#) are obtained from the frequency space data that is generated by incorporating only the exponential term,  $\exp(-t(k_x, k_y)/T_2^*(x, y))$ , in such a way that the FE anomaly weighting function, introduced in [Eq. \(13\)](#), is assumed to be  $W(k_x, k_y, x, y) = \exp(-t(k_x, k_y)/T_2^*(x, y))$ . It can be seen in [Fig. 3\(a<sub>1</sub>\)](#) that the magnitude and real images show blurring and loss of image intensity effect that  $T_2^*$  causes on the edges of the phantom when the considered  $T_2^*$  effect is not corrected. The standard-reconstructed imaginary image shows some artificial imaginary data mostly at the edges of the tissues in the phantom. The modified-reconstructed magnitude, phase, real and imaginary images, that are given in [Fig. 3\(a<sub>2</sub>\)](#), appear to be exactly

the same as the true magnitude, phase, real and imaginary images. This outcome illustrates that  $\Omega_a$  successfully corrects the  $T_2^*$  effect on the reconstructed images.

[Fig. 3.3b<sub>1</sub>](#) illustrates the standard-reconstructed images whereas [Fig. 3\(b<sub>2</sub>\)](#) presents the modified-reconstructed images from the data generated with only  $B$ -field inhomogeneity effects. The frequency space data is generated by considering only the exponential term,  $\exp(-i\gamma\Delta B(x,y)t(k_x,k_y))$ , in such a way that the FE anomaly weighting function in [Eq. \(13\)](#) is assumed to be  $W(k_x,k_y,x,y)=\exp(-i\gamma\Delta B(x,y)t(k_x,k_y))$ . The  $B$ -field inhomogeneity,  $\Delta B$ , is known to produce image warping and bulk shift in the phase encoding direction in magnitude and real images, as it can be seen in [Fig. 3\(b<sub>1</sub>\)](#). Slight warping can also be observed in the vertical frequency encoding direction because of the higher sampling width. As it can be seen in [Fig. 3\(b<sub>1</sub>\)](#),  $B$ -field inhomogeneity introduces artificial imaginary data. It can also be observed that the phase, real, and imaginary images are not uniform as a result of the sinusoidal oscillation due to the linear field map. As seen in the case that we examine  $T_2^*$  effects, the modified-reconstructed images, that are given in [Fig. 3\(b<sub>1</sub>\)](#) have been successfully corrected through  $\Omega_a$ .

Presented in [Fig. 3\(c<sub>1</sub>\)](#) and [Fig. 3\(c<sub>2</sub>\)](#) the standard- and modified-reconstructed images from the data generated with only  $T_1$  recovery term effects. As explained in previous cases, the frequency data generation is performed by assuming that the FE anomaly weighting function in [Eq. \(13\)](#) is  $W(k_x,k_y,x,y)=(1-\exp(-TR/T_1(x,y)))$ . The standard-reconstructed magnitude and real images in [Fig. 3\(c<sub>1</sub>\)](#) exhibit decreased image intensity throughout the phantom. The expected increase in tissue contrast, when the images are modified-reconstructed by the operator,  $\Omega_a$ , are not observable in this simulation since the assumed proton spin density already has significant contrast information. Similarly with the previous results, the modified-reconstructed images have successfully been corrected compared to a standard reconstruction as it is apparent in [Fig. 3\(c<sub>1</sub>\)](#).

[Figs. 3\(d<sub>1</sub>\) and 3\(d<sub>2</sub>\)](#) illustrate the standard- and modified-reconstructed images from frequency space data that is generated with a combination of  $T_2^*$ ,  $\Delta B$ , and  $T_1$ . The effects of all three terms (blurring, image warping and loss of image intensity) can be observed

in the standard-reconstructed images in [Fig. 3\(d<sub>1</sub>\)](#) while the modified-reconstructed images in [Fig. 3\(d<sub>2</sub>\)](#) are same as the true maps.

The correction of FE anomalies can be considered as a means of data processing, and thus could potentially induce artificial correlations. Our proposed model allows one not only to account for their effects but also to compute the exact image-space statistics (mean, variance and correlation). As explained in section 2.1, the correlation matrix produced by [Eq. \(7\)](#) is partitioned into the quadrants that include the correlation between the real components (real/real), between the imaginary components (imaginary/imaginary), and between the real and imaginary components (real/imaginary) of the reconstructed image. Furthermore, the correlations of the magnitude-squared data (square of the magnitude-only data) can be derived from the computed complex-valued correlation matrix and can be considered in the analysis of the correlation structure induced by FE anomaly correction during image reconstruction. In order to present the computed correlation structure, we choose the voxel located in the center of the image as the seed voxel and show the correlation between the measurements of the center voxel, and those from all other voxels. The center voxel's induced magnitude-squared, real/real, imaginary/imaginary, and real/imaginary correlations by the modified FR operator, that are illustrated in [Figs. 4\(a\) and 4\(b\)](#), are produced by superimposing the computed correlation structure of the center voxel on a gray-scale anatomical phantom image. Presented in [Fig. 4\(a\)](#) are the induced correlation maps for the center voxel when  $T_2^*$  is incorporated. Since we have found that separately accounting for  $\Delta B$  and  $T_1$  effects yield the same results, the maps presented in [Fig. 4\(b\)](#) represents the correlation structure induced by  $\Delta B$  or  $T_1$  incorporation. It can be seen that the process of accounting for FE anomalies induces a very small amount of correlation in the maps in [Fig. 4\(a\)](#) and no visible correlation in [Fig. 4\(b\)](#). Since little to no correlation is induced, this FE anomaly correction method is ideal for use in experimental human experiments.

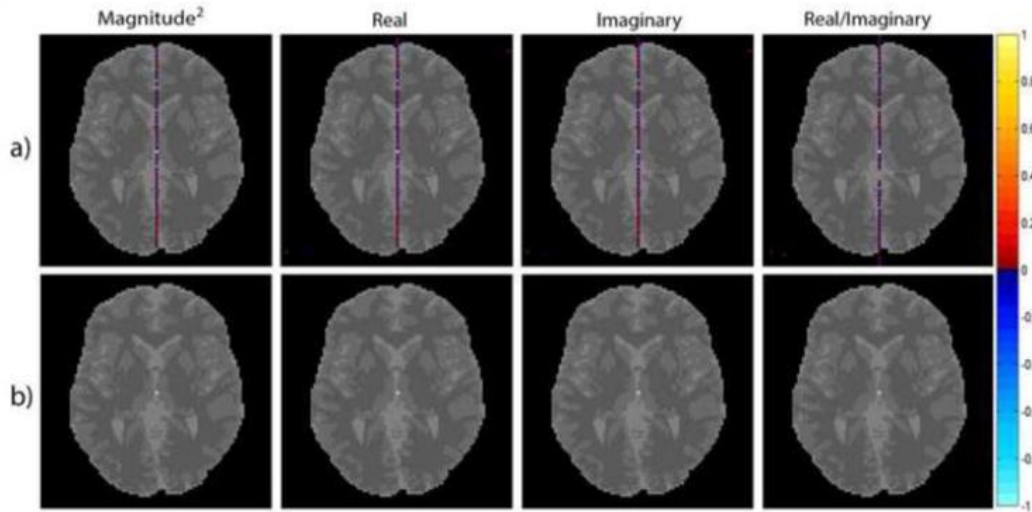


**Fig.4.** Presented on a magnitude brain phantom underlay are theoretical image-space magnitude-squared, real/real, imaginary/imaginary, and real/imaginary correlations about the center voxel induced by the modified Fourier reconstruction operator,  $\Omega_a$ , that accounts for a)  $T_2^*$  effects, b)  $\Delta B$  or  $T_1$  effects. The correlation maps are computed by the linear model,  $corr(y) = D^{-1/2} \Omega_a \Gamma \Omega_a' D^{-1/2}$ , with the assumption of an identity initial spatial covariance,  $\Gamma = I$ , between voxels.

### 3.2. Experimental Illustration

A set of human data from a bilateral finger tapping fMRI block design experiment was acquired for a series of 510 time points with a 3.0 T General Electric Signa LX magnetic resonance imager to further illustrate the performance of the proposed modified FR operator. The data set was comprised of seven 2.5 mm thick axial slices that are 96×96 in dimension for a 24.0 cm FOV, with the phase encoding direction oriented as posterior to anterior (bottom to top in images). The data set had an effective echo spacing of 0.72 ms, a flip angle of 90°, and an acquisition bandwidth of 250 kHz. A time varying TE array was constructed to utilize the resulting signal change that allows for the estimation of the relaxation parameters.<sup>27</sup> The echo time was fixed at 42.7 ms for the first 10 and the last 490 time points, i.e.  $1 \leq t \leq 10$  and  $21 \leq t \leq 510$ . TE values were then equispaced in the interval of [42.7 ms, 52.7 ms] for  $11 \leq t \leq 15$  and  $16 \leq t \leq 20$ .

The application of the proposed linear framework on the acquired data sets is a two-step process, involving the estimation of  $T_2^*$ ,  $T_1$ , and/or  $\Delta B$  followed by the incorporation of the estimates during the image reconstruction with the use of the modified FR

operator. The framework works well when the estimated  $T_2^*$ ,  $\Delta B$ , and  $T_1$  maps are close to the actual maps. The use of underestimated or overestimated parameter maps in the proposed framework can potentially cause undesired artifacts in the reconstructed images. For instance, overcorrection of longer  $T_2^*$  values results in considerable edge enhancements; and the shorter  $T_2^*$  values can suffer from noise amplification [1]. As such, for the experimental illustration of the proposed framework, we focus on incorporation of only  $T_1$  into the FR process since  $T_1$  map can be easily estimated from the measurements acquired during the transient state prior to  $T_1$  equilibrium.<sup>28</sup> However, with accurate estimates of  $T_2^*$  and static  $\Delta B$  maps, the proposed framework can be utilized to incorporate the other Fourier encoding anomalies.

MRI pulse sequences consist of repeated excitation pulses and the magnetization changes in the same way during each repetition. After a number of excitation pulses, the magnetization reaches a steady-state, where the amount of the magnetization at some point in the sequence is the same from one repetition to the next. After reaching the steady-state, the magnetization begins at equilibrium on each repetition. With an assumption of a  $90^\circ$  flip angle, the estimation of  $T_1$  map can be performed from the ratio of the first echo planar imaging time course image and the average steady state image by using a fast  $T_1$  mapping technique introduced in.<sup>28</sup> The steady-state signal for a  $90^\circ$  flip angle is

$$M_{ss} = M_0(1 - e^{-TR/T_1})e^{-TE/T_2^*}, \quad (20)$$

whereas the signal for the first echo planar imaging volume is

$$M_1 = M_0 e^{-TE/T_2^*}. \quad (21)$$

By using the ratio of  $M_1$  in [Eq. \(21\)](#) over  $M_{ss}$  in [Eq. \(20\)](#),  $R = M_1/M_{ss}$ , the value of  $T_1$  for one voxel can be calculated by

$$T_1 = \frac{TR}{\ln\left(\frac{R}{R-1}\right)}. \quad (22)$$

For the estimation of  $T_1$  map from the acquired data set that we use in our experimental illustration, the steady state signal,  $M_{ss}$ , is computed as the average magnitude images at  $6 \leq t \leq 10$  over five time points for each voxel. The estimated  $T_1$  map that is computed by [Eq. \(22\)](#) is shown in [Fig. 5](#). In order to reduce the errors in the final modified-reconstructed images that could result from the  $T_1$  estimation process, the region outside of the brain is masked out in the presented  $T_1$  map. First, the magnitude images at  $21 \leq t \leq 510$  are averaged over the last 490 points of the time series since the data was acquired with a time varying TE in the first 20 time points. In order to generate the binary two-dimensional brain mask that identifies the outside of the brain, the average magnitude image is used as reference. The voxels whose average magnitude values are larger than the threshold value, which is set as the 26% of the maximum value in the average magnitude image, are given a value of 1 (denoting being in the brain) while the voxels whose values are smaller than or equal to this threshold are set to  $10^{-6}$  (denoting being outside the brain) in the binary mask. The estimated  $T_1$  map is then multiplied by the binary mask image on a voxel-by-voxel basis to mask out the voxels in the region outside the brain.



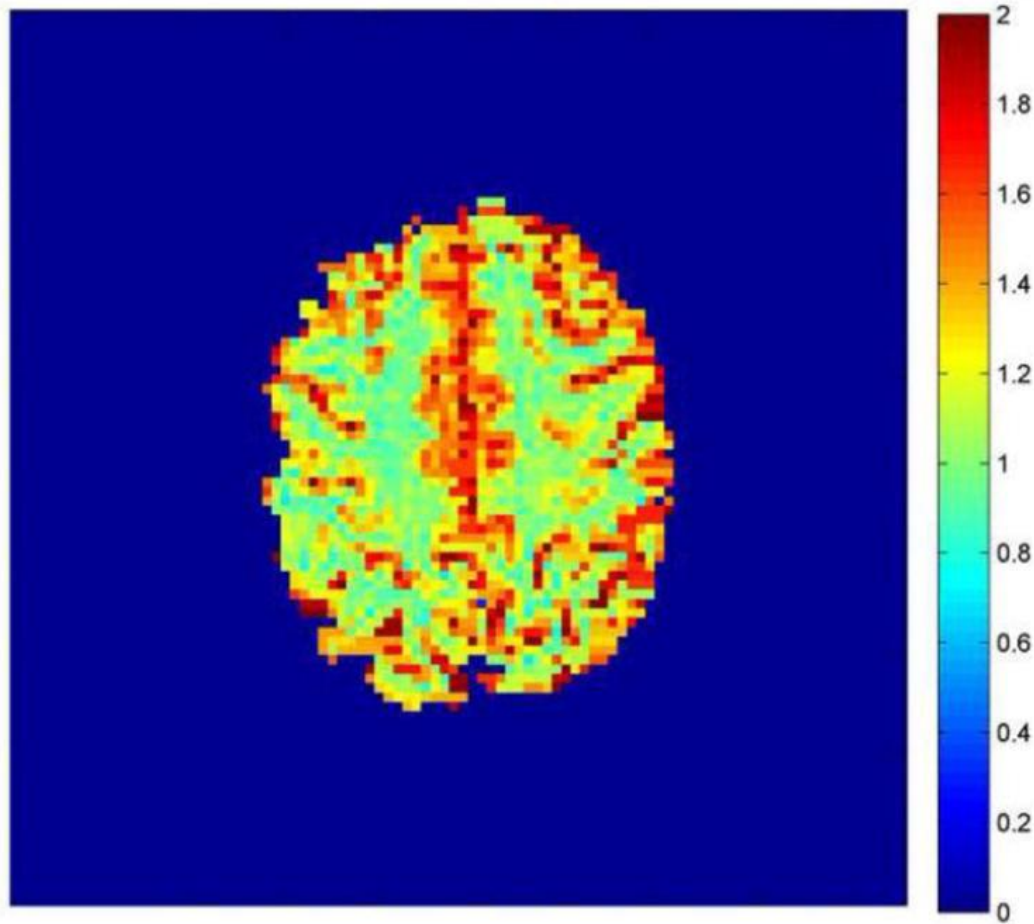


**Fig. 5.** Estimated  $T_1$  map (in s) from the ratio of the first time course image and the average steady state image. The voxel values outside of the brain region are set to  $10^{-6}$  s.

In order to illustrate the benefits of the incorporation of  $T_1$  into the FR process, we show the magnitude, phase, real and imaginary images that are acquired at the 21<sup>st</sup> time point, and reconstructed both with the standard FR operator,  $\Omega$ , and the modified FR operator,  $\Omega_a$ . [Fig. 6\(a\)](#) shows the standard-reconstructed magnitude, phase, real and imaginary images whereas [Fig. 6\(b\)](#) shows the modified-reconstructed images. It can be observed from [Fig. 6](#) that the incorporation of  $T_1$  leads to an increase in image intensity as well as significantly improved tissue contrast in the magnitude images. Such correction does not alter the phase image while increasing the intensity of the magnitude, real, and imaginary images.



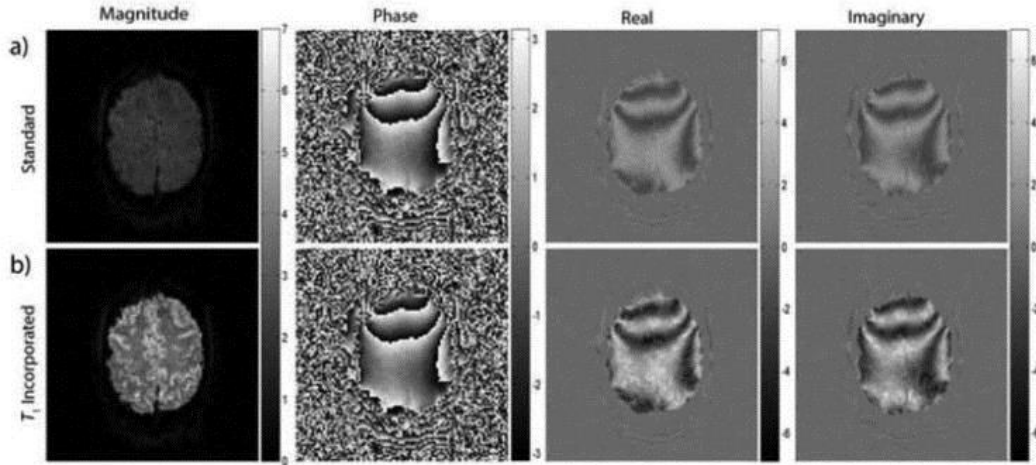


**Fig. 6.** Reconstructed magnitude, phase, real, and imaginary images at time point  $n=21$ . a) Images that are reconstructed with the standard FR operator,  $\Omega$ , b) Images that are reconstructed with the modified FR operator,  $\Omega_a$ .

The increase in image contrast provided by  $T_1$  incorporation can be better observed in [Figs. 7\(a\) and 7\(b\)](#) in which the histogram plots of the magnitude values from gray matter and white matter voxels that were computed before and after incorporation of  $T_1$  are given, respectively. The plots were generated from the voxel values in the magnitude images in the first panels of [Figs. 6\(a\) and 6\(b\)](#). For the segmentation, the estimated  $T_1$  map in [Fig. 5](#) was used, and  $T_1$  ranges were defined predominantly for white matter and gray matter as (0.1 s–1.2 s) and ( $>1.2$  s), respectively. This segmentation resulted in  $n_{WM} = 885$  white matter and  $n_{GM} = 942$  gray matter voxels. By comparing [Figs. 7\(a\) and 7\(b\)](#), one can observe that the contrast between gray matter and white matter regions is significantly improved by the incorporation of  $T_1$  as the white matter and gray matter voxels are more clearly separated in [Fig. 7\(b\)](#) than in [Fig. 7\(a\)](#). This observation is supported by a hypothesis testing analysis for a difference in gray matter and white matter voxel means before and after  $T_1$  incorporation. The test statistic value,  $t^*$ , before  $T_1$  incorporation was found to be 3.29 ( $p$ -value = 0.0012) whereas it was found to be 31.62 ( $p$ -value  $< 10^{-10}$ ) after  $T_1$  incorporation. This strongly implies that the gray-white matter contrast is improved with the use of the proposed method.

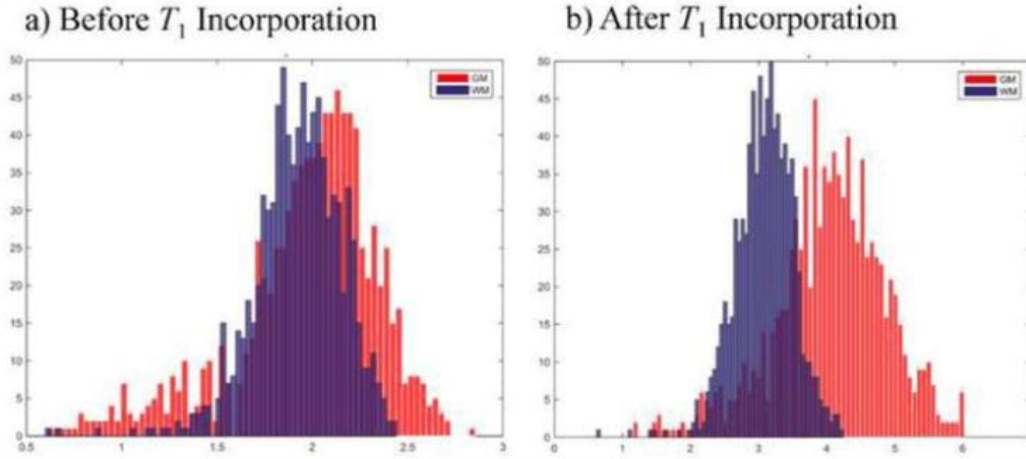


**Fig. 7.** Histogram plots of the magnitude values from gray matter and white matter voxels that are computed a) before incorporation of  $T_1$  and b) after incorporation of  $T_1$ . The plots were generated from the images at time point  $n=21$  that were reconstructed with the standard FR operator,  $\Omega$ , in a) and with the modified FR operator,  $\Omega_a$ , in b).

The contrast enhancement achieved by the proposed method can also be quantitatively indicated by comparing the gray-white matter contrast-to-noise ratio (CNR) computed before and after  $T_1$  incorporation. The gray-white matter CNRs were separately computed from the magnitude images at time point  $n=21$  that were reconstructed with the standard FR operator (given in Fig. 6(a)) and with the modified FR operator that incorporates  $T_1$  (given in Fig. 6(b)). The CNRs were computed from this single image by  $CNR_{GM-WM} = |m_{GM} - m_{WM}|/\sigma_0$ , where  $m_{GM}$  and  $m_{WM}$  are the mean magnitude values of the gray matter and white matter areas, and  $\sigma_0$  is the standard deviation of the outside region. A significant increase in  $CNR_{GM-WM}$  was observed (before: 0.30 and after: 6.08) with the use of our method for  $T_1$  incorporation.

Furthermore, the application of the proposed method for incorporating  $T_1$  was found to yield an increase in signal-to-noise ratios (SNRs) in whole brain as well as gray and white matter areas as presented in Table 2. The SNR values in Table 2 were computed by  $SNR = m_{ROI}/\sigma_0$ , where  $m_{ROI}$  is the mean magnitude value of the region of interest (whole brain, gray matter or white matter in the table). Our results show that  $T_1$  incorporation increases the SNR by 83%, 105%, and 60% in whole brain, gray matter, and white matter areas, respectively for the single image that was chosen for the analysis.

**Table 2.** Signal-to-noise ratios of the whole-brain, gray matter, and white matter areas before and after  $T_1$  incorporation

	Whole-brain	Gray Matter	White Matter
<b>Before <math>T_1</math> Incorporation</b>	8.06	8.20	8.00
<b>After <math>T_1</math> Incorporation</b>	14.76	16.82	12.83

In order to analyze the possible effects of such correction on the functional activations computed from  $T_1$  incorporated reconstructed images, we show the activation statistics of both standard-reconstructed and modified-reconstructed images in [Figs. 8\(a\), 8\(c\) and 8\(b\), 8\(d\)](#), respectively. [Figs. 8\(a\) and 8\(b\)](#) show the activation  $t$ -statistics computed by using the likelihood ratio tests from the MO Model.<sup>21</sup> Illustrated in [Figs. 8\(c\) and 8\(d\)](#) are the activation Z-statistics computed by using the CV Model.<sup>22-25</sup> The activation maps shown in [Fig. 8](#) were thresholded at a 5% per comparison error rate<sup>29</sup> and presented with a color bar that ranges between -6.5 and 6.5. It can be observed that the activation statistics that are computed from the standard-reconstructed and the modified-reconstructed image space measurements are identical for both the CV and MO Models. It can be concluded that  $T_1$  incorporation into the Fourier image reconstruction process preserves the functional activations. This result is expected since the estimated  $T_1$  map that is incorporated during the image reconstruction is constant over the time series and therefore the activation information is preserved with the proposed framework.

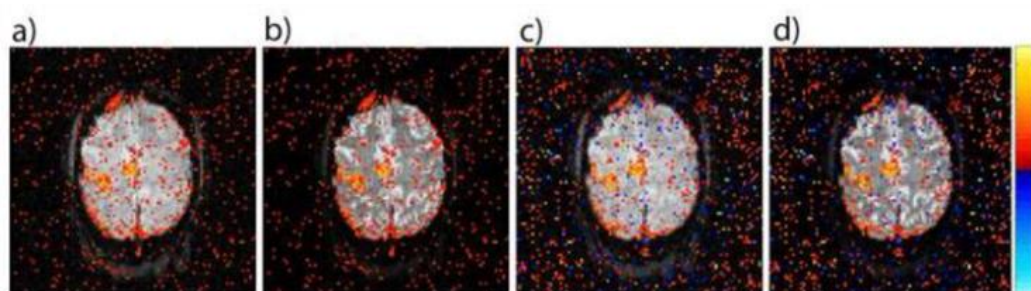


**Fig.8.** Activation statistics that are computed from a) standard-reconstructed images with the use of the MO Model, b) modified-reconstructed with the use of the MO Model, c) standard-reconstructed images with the use of the CV Model, d) modified-reconstructed with the use of the CV Model. The activation maps are thresholded at a 5% per comparison error rate.

## 4. Conclusion

The model developed in this work is based upon the mathematical linear framework for Fourier image reconstruction in a real-valued isomorphism presented in<sup>17</sup> and expanded to the AMMUST- $k$  framework in order to include frequency space processing operations in.<sup>18</sup> We further expand this framework to account for the effects of relaxation parameters,  $T_2^*$  and  $T_1$ , and magnetic field inhomogeneities,  $\Delta B$ , that alters the observed MR signal in the process of Fourier encoding. We develop a modified FR operator that accounts for such effects in image space by first generating the modified FE operator that considers the terms of these anomalies as they appear in the signal equation, and then inverting. Although the effects of  $T_2^*$  and  $\Delta B$  have been aimed to be corrected prior to the final analysis of fMRI data in previous studies, the  $T_1$  recovery term has been ignored with the assumption of long repetition time, which is not always met, especially when performing fast repetitive excitations. Furthermore, the  $T_1$  estimates have the potential to detect tissue characteristics of the acquired MRI data.

We present theoretical results for accounting for the effects of  $T_2^*$ ,  $\Delta B$ , and  $T_1$  during the Fourier reconstruction process, and focus on incorporating  $T_1$  in acquired echo planar data. The experimental results presented in this manuscript have shown that the images reconstructed through the use of the reconstruction operator adjusted for estimated static  $T_1$  appear to be brighter and have increased tissue contrast. The method presented in this work can provide improved tissue segmentation over the course of time series, and as suggested in prior studies,<sup>13-16</sup> this increased gray/white matter contrast can improve the precision of motion correction and image registration. Furthermore, our experimental results show that such correction does not alter the activation results in an EPI based BOLD fMRI experiment. Even though we incorporate only  $T_1$  into the reconstruction process in experimental analysis, the model can be utilized to account for  $T_2^*$  and  $\Delta B$  effects once their estimated maps are obtained.

The proposed framework makes it possible to precisely quantify any potential induced correlations by the process of accounting for FE anomalies. It has been shown that  $\Delta B$  and  $T_1$  incorporation do not

induce any image space correlations whereas accounting for  $T_2^*$  effect induces negligible correlation in the phase encoding direction. The FA correction methods introduced in this manuscript can be used on a regular basis in every fMRI and fcMRI experiment.

As noted before, the proposed method requires an additional step of estimating  $T_1$ ,  $T_2^*$ , and/or  $\Delta B$  before performing the incorporation of the anomalies into the reconstruction process. Variations in the RF transmit field can cause non-uniform  $B_1$  field strengths creating flip angle variations over the field of view that can lead to non-uniformities across the MRI image and thus errors in image-based quantitative measurements, including  $T_1$  estimation. Inaccuracy of the estimated  $T_1$  map as a result of non-uniformity in  $B_1$  field, especially at high field strength, could potentially reduce the benefit of the proposed method as the  $T_1$  incorporated reconstructed images could be inaccurate. One possible solution to this problem is to produce an accurate map of the non-uniform  $B_1$  field map and correct the intensity inhomogeneities that arise from  $B_1$  non-uniformity<sup>30-33</sup> before performing  $T_1$  estimation.

Recovering image contrast in EPI acquisitions by incorporating  $T_1$  with the use of the proposed framework can be specifically useful for 3D EPI fMRI acquisitions which provide higher temporal SNR and stronger statistical power in activation detection. As 3D EPI yields increased  $T_1$  contrast between tissue types due to the short TR and thus more accurate  $T_1$  estimation, the benefits of our proposed method can be significantly observed in 3D EPI experiments. The method provides higher signal characteristics, such as increased SNR and gray-white matter CNR, more detailed structural information in the reconstructed images, and ultimately reduction in the registration errors in one step from a single pulse sequence as it does not require the acquisition of the anatomical  $T_1$ -weighted data.

## Acknowledgments

This work was supported by NIH NS087450. The digital phantom that is used to present theoretical illustration results in this manuscript was provided by Volkan Emre Akpinar from the Department of Neurosurgery at Medical College of Wisconsin in Milwaukee, WI.

## Footnotes

*Magnetic Resonance Imaging*, Vol 33, No. 4 (May 2015): pg. 374-384. [DOI](#). This article is © Elsevier and permission has been granted for this version to appear in [e-Publications@Marquette](mailto:e-Publications@Marquette). Elsevier does not grant permission for this article to be further copied/distributed or hosted elsewhere without the express permission from Elsevier.

**Publisher's Disclaimer:** This is a PDF file of an unedited manuscript that has been accepted for publication. As a service to our customers we are providing this early version of the manuscript. The manuscript will undergo copyediting, typesetting, and review of the resulting proof before it is published in its final citable form. Please note that during the production process errors may be discovered which could affect the content, and all legal disclaimers that apply to the journal pertain.

## References

1. Stroman PW. *Essentials of functional MRI*. Florida: CRC Press; 2011.
2. Haacke EM, Brown R, Thompson M, Vankatesan R. *Magnetic resonance imaging: Physical principles and sequence design*. New York: John Wiley and Sons; 1999.
3. Jezzard P, Balaban RS. Correction for geometric distortion in echo planar images from B0 field variations. *Magn Reson Med*. 1995;34:65–73.
4. Reber PJ, Wong EC, Buxton RB, Frank LR. Correction of off resonance-related distortion in echo-planar imaging using EPI-based field maps. *Magn Reson Med*. 1998;39:328–330.
5. Kannengiesser SA, Wang Y, Haacke EM. Geometric distortion correction in gradient-echo imaging by use of dynamic time warping. *Magn Reson Med*. 1999;42:585–590.
6. Hahn AD, Rowe DB. Physiologic noise regression, motion regression, and TOAST dynamic field correction in complex-valued fMRI time series. *Neuroimage*. 2012;59:2231–2240.
7. Hahn AD, Nencka AS, Rowe DB. Enhancing the utility of complex-valued functional magnetic resonance imaging detection of neurobiological processes through postacquisition estimation and correction of dynamic B0 errors and motion. *Hum Brain Mapp*. 2012;33:288–306.
8. Maclaren JR, Bones PJ, Millane RP, Watts R. MRI with TRELLIS: a novel approach to motion correction. *Magn Reson Imag*. 2008;26:474–483.
9. Bernstein MA, King KF, Zhou XJ. *Handbook of MRI Pulse Sequences*. Burlington: Elsevier; 2004.
10. Zhou XJ, Liang Z, Cofer GP, Beaulieu CF, Suddarth SA, Johnson G. Reduction of ringing and blurring artifacts in fast spin-echo imaging. *Magn Reson Imag*. 1993;3:803–807.
11. Robitaille P, Berliner L. *Ultra High Field Magnetic Resonance Imaging*. Berlin: Springer; 2007.
12. Mazaheri Y, Biswal BB, Ward BD, Hyde JS. Measurements of tissue T1 spin lattice relaxation time and discrimination of large draining veins using transient EPI data sets in BOLD-weighted fMRI acquisitions. *Neuroimage*. 2006;32:603–15.



13. Saad ZS, Glen DR, Chen G, Beauchamp MS, Desai R, Cox RW. A new method for improving functional-to-structural MRI alignment using local Pearson correlation. *Neuroimage*. 2009;44:839–848.
14. Rowland DJ, Garbow JR, Laforest R, Snyder AZ. Registration of [F-18] FDG microPET and small-animal MRI. *Nuclear Medicine and Biology*. 2005;32:567–572.
15. Vaquero JJ, Desco M, Pascau J, Santos A, Lee I, Seidel J, Green MV. PET, CT, and MR image registration of the rat brain and skull. *IEEE Transactions on Nuclear Science*. 2001;48:1440–1445.
16. Gonzalez-Castillo J, Duthie KN, Saad ZS, Chu C, Bandettini PA, Luh W. Effects of image contrast on functional MRI image registration. *Neuroimage*. 2013;67:163–174.
17. Rowe DB, Nencka AS, Hoffman RG. Signal and noise of Fourier reconstructed fMRI data. *J Neurosci Meth*. 2007;159:361–369.
18. Nencka AS, Hahn AD, Rowe DB. A mathematical model for understanding statistical effects of k-space (AMMUST-k) preprocessing on observed voxel measurements in fcMRI and fMRI. *J Neurosci Meth*. 2009;181:268–282.
19. Bruce IP, Karaman MM, Rowe DB. A statistical examination of the SENSE reconstruction via an isomorphism representation. *Magn Reson Imag*. 2011;29:1267–1287.
20. Karaman MM, Nencka AS, Bruce IP, Rowe DB. Quantification of the Statistical Effects of Spatiotemporal Processing of Non-task fMRI Data. *Brain Connectivity*. 2014;4(9):649–661.
21. Bandettini PA, Jesmanowicz A, Wong EC, Hyde JS. Processing strategies for time course data sets in functional MRI of the human brain. *Magn Reson Med*. 1993;30:161–173.
22. Rowe DB, Logan BR. A complex way to compute fMRI activation. *Neuroimage*. 2004;23:1078–1092.
23. Rowe DB. Parameter estimation in the magnitude-only and complex-valued fMRI data models. *Neuroimage*. 2005;25(4):1124–1132.
24. Rowe DB. Modeling both the magnitude and phase of complex-valued fMRI data. *Neuroimage*. 2005;25:1310–1024.
25. Rowe DB. Magnitude and phase signal detection in complex-valued fMRI data. *Magn Reson Med*. 2009;62(5):1356–1357.
26. Atlas SW. *Magnetic Resonance Imaging of the Brain and Spine*. Lippincott, PA: Williams & Wilkins; 2008.
27. Karaman MM, Bruce IP, Rowe DB. A Statistical fMRI Model for Differential  $T_2^*$  Contrast Incorporating  $T_1$  and  $T_2^*$  of Gray Matter. *Magn Reson Imag*. 2014;32(1):9–27.
28. Bodurka J, Ye F, Petridou N, Murphy K, Bandettini PA. Mapping the MRI voxel volume in which thermal noise matches physiological noise- Implications for fMRI. *Neuroimage*. 2007;34:542–49.

29. Logan BR, Rowe DB. An evaluation of thresholding techniques in fMRI analysis. *Neuroimage*. 2004;22:95–108.
30. Mihara H, Iriguchi N, Ueno S. A method of RF inhomogeneity correction in MR imaging. *Magn Reson Mater Phys Biol Med*. 1998;7:115–120.
31. Trejer R, Steingoetter A, Fried M, Schwizer W, Boesiger P. Optimized and combined T1 and B1 mapping technique for fast and accurate T1 quantification in contrast-enhanced abdominal MRI. *Magn Reson Med*. 2007;57:568–576.
32. Volz S, Noth U, Rotarsa-Jagiela A, Deichmann R. A fast  $B_1$  mapping method for the correction and normalization of magnetization transfer ratio maps at 3 T. *Neuroimage*. 2010;49:3015–3026.
33. Wang J, Qiu M, Yang QX, Smith MB, Constable RT. Measurement and correction of transmitter and receiver induced non-uniformities in vivo. *Magn Reson Med*. 2015;53:408–417.